ISAR IMAGING BY EXPLOITING THE CONTINUITY OF TARGET SCENE

Lu Wang, Lifan Zhao, Guoan Bi, *Liren Zhang*

School of EEE, NTU
Singapore

UAE University
UAE

ABSTRACT

Compressive sensing (CS) based Inverse Synthetic Aperture Radar (ISAR) imaging exploits the sparsity of the target scene to achieve high resolution and effective denoising with limited measurements. This paper extends the CS based ISAR imaging to further include the continuity structure of the target scene within a Bayesian framework. A correlated prior is imposed to statistically encourage the continuity structures in both the cross-range and range domains of the target region and the Gibbs sampling strategy is used for Bayesian inference. Because the resulted method requires to recover the whole target scene at a time with heavy computational complexity, an approximate strategy is proposed to alleviate the computational burden. Experimental results demonstrate that the proposed algorithm can achieve substantial improvements in terms of preserving the weak scatterers and removing noise over other reported CS based ISAR imaging algorithms.

Index Terms— model-based compressive sensing, ISAR imaging, continuity structures

1. INTRODUCTION

The CS based radar imaging has received much attention due to its ability of achieving high resolution range or cross-range profile with limited measurements. These techniques have been intensively studied in [1–7] where different sparse recovery methods have been used in ISAR/SAR imagery applications. The l_1-norm minimization based Basis Pursuit (BP) is employed to obtain the ISAR images with high-resolution [2] [3]. Apart from sparsity, additional constraint such as Total Variation (TV), may be added [4] to deal with speckle noise in SAR imaging. The Matching Pursuit (MP) is used for imagery of the target with uniform or even maneuvering rotation [5] due to its computational efficiency and the Bayesian Compressive Sensing (BCS) strategy has been found to obtain an auto-focused ISAR image [6] and high-resolution SAR image [7].

In most literature of the CS based ISAR imagery, undersampling is performed in the cross-range domain for each range cell after the pulse compression [2]. Assuming that the translational motion has been fully removed by motion compensation, it is shown in [2] that the signal model follows:

$$\mathbf{Y} = \mathbf{ADX} + \varepsilon \tag{1}$$

where $\mathbf{Y} \in \mathcal{C}^{L\times N}$ with $\mathbf{y}_{:,n}$ for $n = 1 : N$ representing the measurements in the nth range cell; $\mathbf{X} \in \mathcal{C}^{M\times N}$ is the sparse coefficient matrix capturing the complex amplitudes of the scatterers on the target scene of interest; $\mathbf{D} \in \mathcal{C}^{M\times M}$is the Fourier dictionary,

$$\mathbf{D} = [\mathbf{d}_1\, \mathbf{d}_2 \cdots \mathbf{d}_M] \,,$$

with

$$\mathbf{d}_m = \exp\left(-j2\pi f_m \mathbf{t}\right),$$

where $\mathbf{t}^T = 1/f_r[1 : M]$, M is the number of pulses, $f_m = f_r/M(m-1)$ with $m = 1 : M$ and f_r is the pulse repetition frequency. In Eq. (1), $\mathbf{A}$ is the sensing matrix of size $L \times M$ with $L < M$ and ε is the additive noise. It is proposed in [2] to employ the BP method to solve the imaging problem:

$$\min_{\mathbf{x}_{:,n}} \left(\|\mathbf{x}_{:,n}\|_1\right) \;\; \textit{subject to} \; \|\mathbf{y}_{:,n} - \mathbf{AD}\mathbf{x}_{:,n}\|_2 \le \lambda\sigma \tag{2}$$

where λ is the user-selected regularization parameter and σ is the noise power. Other signal models without range compression derived in [3] for ISAR and [7] for SAR allow undersampling in both the range and the cross-range domains. However, since the model in [3] requires to recover the whole target image, the resulted unknown high dimensional vector induces a heavy burden of computations. We focus on undersampling in cross-range domain and use the model (1).

In contrast to the conventional CS based ISAR imaging, the continuity structures of the target scene is taken into consideration in this paper. The continuity structure is statistically imposed by using a correlated prior for the sparse coefficients and the Gibbs sampling strategy is used for Bayesian inference. Since sparse coefficients of one range cell become correlated with those of other range cells, the resulted algorithm also requires to recover the whole target scene at a time. To alleviate the high computation burden, an approximate strategy is proposed by considering merely the measurements from the neighboring range cells. Results from the real data experiments have demonstrated that the proposed approximate imaging method outperforms the conventional CS based ISAR imaging methods particularly in preserving the weak target scatterers.

978-1-4799-2893-4/14/$31.00 ©2014 IEEE

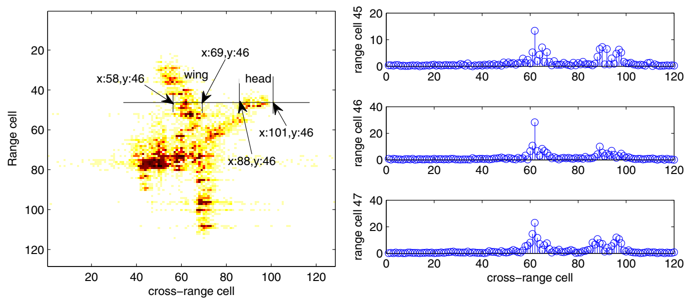

(a) Image by RDA (b) Profiles

Fig. 1. Continuity structure illustration by Yak-42. The radar system parameters are given in Section 5.

2. MOTIVATION

The motivation for considering the continuity structures of the range and cross-range of the target scene into ISAR imagery is illustrated by the real data image of Yak-42 airplane. The image obtained by the Range Doppler algorithm (RDA) [8] with full measurements is given in Fig. 1 (a) where the scatterers obviously exhibit a sparse property.

In addition to sparsity, continuities in cross-range and range domains can be observed. Figure. 1 (b) shows the profiles of range cells 45, 46 and 47. An example of the continuity in cross-range is clearly shown in each range cell where the scatterers with nonzero magnitude are grouped in two clusters corresponding to the head and the wing of the plane, respectively. The continuity in range domain is shown by the fact that the scatterers of the neighboring range cells 45, 46 and 47 tend to be nonzero or zero almost simultaneously. A closer inspection of the scatter points in cross-range cell 63 and range cell 46 shows that both the continuities in range and cross-range are demonstrated simultaneously. Motivated by this phenomenon, three continuity patterns are summarized in Fig. 2. If any of the patterns in Fig. 2 is observed, it is reasonable to assume that $x_{m,n}$ is nonzero with a high probability. Therefore the continuity either in range domain, cross-range domain, or in both domains can be encouraged accordingly.

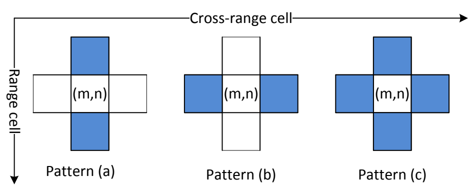

Fig. 2. Continuity patterns: shaded squares denote the scatterers with nonzero amplitudes and the white ones are the scatterers which are irrelevant to the scatterer (m, n).

3. MODEL-BASED ISAR IMAGING

To incorporate the continuity structures into ISAR imagery, problem (1) is reformulated under the Bayesian framework. Let $\mathbf{x} = \mathbf{vec}(\mathbf{X})$ be the vectorized $\mathbf{X}$ by columns and accordingly we abuse the subscripts i and m, n for simple representation. Following [9] [10], let x_i or $x_{m,n}$ follow a Bernoulli-Gaussian distribution, also known as a "spike-and-slab" prior to encourage sparsity, i.e.,

$$p(\mathbf{x}\,|\mathbf{q},\beta\,) = \prod_{i=1}^{MN}\left[(1-q_i)\delta(|x_i|) + \frac{q_i\beta_i}{\pi}\exp(-\beta_i|x_i|^2)\right], \quad (3)$$

where hyper-parameter q_i is the prior probability of x_i being nonzero, β_i is the precision of x_i, $\beta^T = [\beta_1, \ldots, \beta_{MN}]$ and $\mathbf{q}^T = [q_1, \ldots, q_{MN}]$.

3.1. Priors for β and q

To enforce continuity patterns in both range and cross-range domains in Fig. 2, it is proper to choose a correlated prior for the precisions of $x_{m,n}$ and its four neighbors.To obtain a tractable posterior of $\beta_{m,n}$, we further impose a Gamma prior $\mathrm{Gamma}\,(b, d)$ on $\beta_{m,n}$, which is conjugate to Gaussian distribution. The posterior of $\beta_{m,n}$ given $\mathbf{x}$ then follows a Gamma distribution with different parameters for different patterns:

$$p\,(\beta_{m,n}\,|\mathbf{x}, b, d\,) = \begin{cases} \text{Gamma}(b+5, d + \|\bar{\mathbf{x}}_{m,n}\|_2^2) \\ \text{Gamma}(b+3, d + \|\bar{\mathbf{x}}^k_{m,n}\|_2^2) \end{cases} \quad (4)$$

where $k = 1, 2$, $\bar{\mathbf{x}}^1_{m,n} = [x_{m-1,n}\, x_{m+1,n}\, x_{m,n}\,]^T$ for pattern (a), $\bar{\mathbf{x}}^2_{m,n} = [x_{m,n}\, x_{m,n-1}\, x_{m,n+1}]^T$ for pattern (b) and $\bar{\mathbf{x}}^T_{m,n} = [x_{m-1,n}\; x_{m+1,n}\; x_{m,n}\; x_{m,n-1}\; x_{m,n+1}]$ for pattern (c).

Based on the idea of continuity, three kinds of sparsity patterns are introduced to infer $\mathbf{q}$. They are the patterns for strong acception, strong rejection and weak rejection.
Strong rejection : If $\bar{\mathbf{x}}_{m,n} \backslash x_{m,n}$, i.e., the sub-vector of $\bar{\mathbf{x}}_{m,n}$ excluding element $x_{m,n}$, are all zeros, it is highly possible that $x_{m,n}$ is zero due to the continuity assumption. Therefore, prior $Beta(e_0, f_0)$ with $e_0 < f_0$ is used to encourage $q_{m,n}$ being small to reject scatterer (m, n).
Strong acception: If any of the continuity patterns in Fig. (2) is observed, then it is highly possible that $x_{m,n}$ is nonzero. Then prior $Beta(e_2, f_2)$ with $e_2 > f_0$ is used to encourage $q_{m,n}$ being large to accept scatterer (m, n).
Weak rejection: Apart from those sparsity patterns mentioned, no apparent conclusion can be drawn on the value of $q_{m,n}$. The prior $Beta(e_1, f_1)$ with $e_1 = f_1$ is used to exert non-informative prior on the $q_{m,n}$.

To summarize, a Beta distribution with three different sets of parameters $\{e_k, f_k\}_{k=0,1,2}$, is assigned for $q_{m,n}$ according to the introduced sparsity patterns to facilitate the inference. Since Beta distribution is conjugate to Bernoulli distribution for the unknown variable $q_{m,n}$, the posterior for $q_{m,n}$ is a Beta distribution,

$$\begin{array}{l} p\left(q_{m,n}^{k} \left| \mathbf{x}, e_k, f_k \right.\right) = p\left(q_{m,n}^{k} \left| \bar{\mathbf{x}}_{m,n}, e_k, f_k \right.\right) \\ = \mathbf{Beta}\left(e_k + \left\| \bar{\mathbf{x}}_{m,n} \right\|_0, f_k + 5 - \left\| \bar{\mathbf{x}}_{m,n} \right\|_0\right) \end{array}, \tag{5}$$

where $k \in \{0, 1, 2\}$ and $\|\mathbf{x}\|_0$ denotes the number of the nonzero components in $\mathbf{x}$.

3.2. Posteriors

Assuming that ε follows a complex white Gaussian distribution with zero mean and unknown precision β_0, i.e., $\varepsilon \sim \mathcal{CN}\left(\mathbf{0}, \beta_0^{-1}\mathbf{I}\right)$, the posterior distribution of all the variables given $\mathbf{y} = \mathbf{vec}(\mathbf{Y})$ follows

$$\begin{array}{l} p\left(\mathbf{x}, \mathbf{q}, \beta, \beta_0 \left| \mathbf{y} \right.\right) \\ \propto p\left(\mathbf{y} \left| \Phi\mathbf{x}, \beta_0 \right.\right) p\left(\beta_0\right) p\left(\mathbf{x} \left| \mathbf{q}, \beta \right.\right) p\left(\mathbf{q}\right) p\left(\beta\right), \end{array} \tag{6}$$

where $\Phi \in \mathcal{C}^{NL \times MN}$ represents $\mathbf{diag}\{\mathbf{AD}, \ldots, \mathbf{AD}\}$ with ϕ_i being the i-th column and $\mathbf{diag}\{\mathbf{AD}, \ldots, \mathbf{AD}\}$ denotes a block diagonal matrix with principal diagonal blocks being $\mathbf{AD}$. Equation. (6) is intractable due to the implicit priors for β and $\mathbf{q}$ and no analytical estimation can be found for the unknowns. The Gibbs sampler [11] is used to generate samples asymptotically distributed according to (6) and to obtain the estimation of $\{\mathbf{x}, \mathbf{q}, \beta, \beta_0\}$. To ensure a tractable posterior distribution $p\left(\beta_0 \left| \mathbf{x}, \mathbf{y} \right.\right)$ of β_0, it is assumed that β_0 follows a Gamma distribution, $Gamma(b_n, d_n)$. Due to conjugacy, it is seen

$$p\left(\beta_0 \left| \mathbf{x}, \mathbf{y} \right.\right) = \mathrm{Gamma}\left(b_n + NL, d_n + \left\| \mathbf{y} - \Phi\mathbf{x} \right\|_2^2\right). \tag{7}$$

Based on (6), the posterior distribution of $\mathbf{x}$ is proportional to

$$\begin{array}{l} p\left(\mathbf{x} \left| \mathbf{y}, \mathbf{q}, \beta, \beta_0 \right.\right) \propto p\left(\mathbf{y} \left| \Phi\mathbf{x}, \beta_0 \right.\right) \\ \times \left\{ \prod\limits_{i}^{MN} \left[\left(1 - q_i\right) \delta\left(\left| x_i \right|\right) + \frac{q_i \beta_i}{\pi} \exp\left(-\beta_i \left| x_i \right|^2\right) \right] \right\} \end{array}. \tag{8}$$

From (8), one can easily compute the posterior distribution of x_i given $\{\mathbf{x} \backslash x_i, \mathbf{y}, \mathbf{q}, \beta, \beta_0\}$ for $1 \le i \le MN$, which follows

$$\begin{array}{l} p\left(x_i \left| \mathbf{x} \backslash x_i, \mathbf{y}, \mathbf{q}, \beta, \beta_0 \right.\right) \propto \\ \quad \left(1 - \tilde{q}_i\right) \delta\left(\left| x_i \right|\right) + \tilde{q}_i \mathcal{CN}\left(x_i \left| \tilde{\mu}_i, \tilde{\beta}_i^{-1} \right.\right) \end{array} \tag{9}$$

where

$$\tilde{\beta}_i = \beta_i + \beta_0 \phi_i^H \phi_i,$$

$$\tilde{\mu}_i = \tilde{\beta}_i^{-1} \beta_0 \phi_i^H \left(\mathbf{y} - \sum_{j=1, j \ne i}^{MN} x_j \phi_j \right),$$

$$\frac{\tilde{q}_i}{1 - \tilde{q}_i} = \frac{q_i}{1 - q_i} \times \frac{\mathcal{CN}\left(0, \beta_i^{-1}\right)}{\mathcal{CN}\left(\tilde{\mu}_i, \tilde{\beta}_i^{-1}\right)}.$$

3.3. ISAR Imaging Algorithm and its Approximation

The estimate of $\mathbf{x}$ is empirically given by averaging the last few samples of the Gibbs sampler and the successive steps are summarized in Algorithm 1. The convergence of the Gibbs sampler is generally hard to diagnose. However, empirical experiments show that the algorithm converges after several dozens of iterations. As shown in Algorithm 1, the proposed algorithm recovers the whole target scene $\mathbf{X}$ at a time due to the dependent prior. Comparing to the method in [2] where the profiles in different range cells are recovered individually, the proposed method suffers a high computational burden. To alleviate the computational complexity, we suggest to parallelly recover the profiles in different range cells. Only the profile in one range cell is recovered at a time using the measurements of its own and its two neighbors. The resulted approximate algorithm is illustrated in Fig. 3 and summarized in Algorithm 2. In this way, we not only decrease the computational complexity, but also incorporate the continuity structure in the imagery process.

Algorithm 1 Gibbs sampler

Initialize the maximum iteration number $N_{Maxiter}$, iteration counter $l = 0$ and initial value of $\{\beta, \mathbf{q}, \beta_0, b, d, b_n, d_n, e_k, f_k\}$.
while $l \le N_{Maxiter}$ **do**
  for $i = 1 : MN$ **do**
    Sample x_i according to $p\left(x_i \left| \mathbf{x} \backslash x_i, \mathbf{y}, \mathbf{q}, \beta, \beta_0 \right.\right)$ (9);
    Sample β_i according to $p\left(\beta_{m,n} \left| \mathbf{x}, b, d \right.\right)$ (4);
    Sample q_i according to $p\left(q_{m,n}^{k} \left| \mathbf{x}, e_k, f_k \right.\right)$ (5);
  end for
  Sample β_0 according to $p\left(\beta_0 \left| \mathbf{x}, \mathbf{y} \right.\right)$ (7).
end while
$\hat{\mathbf{x}}$ and $\hat{\beta}_0$ are obtained by the empirical mean of the samples of $\mathbf{x}$ and β_0 in the last few iterations, respectively.

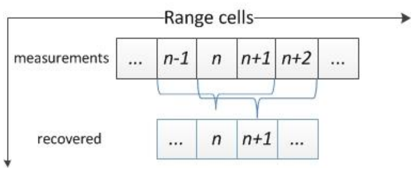

Fig. 3. Approximate algorithm illustration.

Algorithm 2 Approximate algorithm

for $n = 1 : N$ **do**
  Gibbs sampler in Algorithm 1 with
  $\mathbf{x} = \mathbf{vec}(\mathbf{X}_{:,n-1:n+1})$, $\mathbf{y} = \mathbf{vec}(\mathbf{Y}_{:,n-1:n+1})$
  $\Phi = \mathbf{diag}\{\mathbf{AD}, \mathbf{AD}, \mathbf{AD}\}$
end for
The estimated target scene is given by $\hat{\mathbf{X}}_{:,1:N}$.

4. RELATION TO PRIOR WORK

As mentioned in Section 1, conventional CS based imaging algorithms merely consider the sparsity property to recover the target scene with measurements down-sampled from cross-range [2], range [3] or both domains [7]. However, since only the strong scatterers are preserved by the conventional CS based methods, the recovered target scene is too sparse. Despite sparsity, the proposed ISAR imaging algorithm exploits the continuities of both range and cross range of the target scene by leveraging the model-based CS [12] which exploits the inherent signal structure under the Bayesian framework. Similar ideas have been used for recovering a tree-structured sparse signal [9] and one dimensional sparse signal with cluster structure [10]. To the best of our knowledge, employing the continuity structure in the CS-based ISAR imaging is discussed for the first time in our paper. Algorithm 1 is an extension of [10] into two dimensions. Since Algorithm 2 locally enforces the continuity of target scene using only measurements in 3 neighboring range cells, the continuity structure is not fully exploited. Its computational complexity is relatively larger than that reported in [10] but is much smaller than that of Algorithm 1 as summarized in Table. 1.

Table 1. Comparison of the computational complexities

Algorithm 1	$O\left(LMN^2N_{Maxiter}\right)$
Algorithm 2	$O\left(3NLMN_{Maxiter}\right)$
Method [10]	$O\left(NLMN_{Maxiter}\right)$

5. REAL DATA EXPERIMENTS

In this section, practical data experimental results obtained by the proposed approximate imaging algorithm (Algorithm 2), the conventional CS based methods, such as the BP and the BCS, and the CluSS [10] are compared. The data used is "Yak-42" plane dataset with parameters given as follows: the carrier frequency is 10GHz; $f_r = 25$Hz; the bandwidth is 400MHz.The number of points in the range domain is 128 and 128 pulses are measured. Assuming that the original dataset is noiseless, additional complex white Gaussian noise is added to generate the experimental data with a signal to noise ratio (SNR) of 10dB. Algorithms are tested with $1/2$ of the full measurements, i.e., 64 measurements and the results are provided in Fig. 4. As seen in Fig. 4, all methods can properly recover most of the strong scatterers. However, comparing to those obtained by the BCS and the BP, the images obtained by our method and the CluSS are much more concentrated with relatively clear background. Since the CluSS merely considers the continuity in cross-range domain, it is relatively inferior to the proposed method in preserving the weak scatterers.

Image entropy and the correlation value with the reference image in Fig. 1 (a) are two measures to quantitively evaluate the quality of the recovered images. Note that the higher the correlation value a method provides, the better the method preserves the information of the target. The more focused the image is, the smaller its entropy will be. The correlation and the entropy values of the obtained images by different methods are summarized in Table 2. As indicated in Table 2, the results obtained by the proposed approximate algorithm and the CluSS achieve a higher correlation with the reference image and a lower image entropy than those given by the conventional CS-based imaging methods.

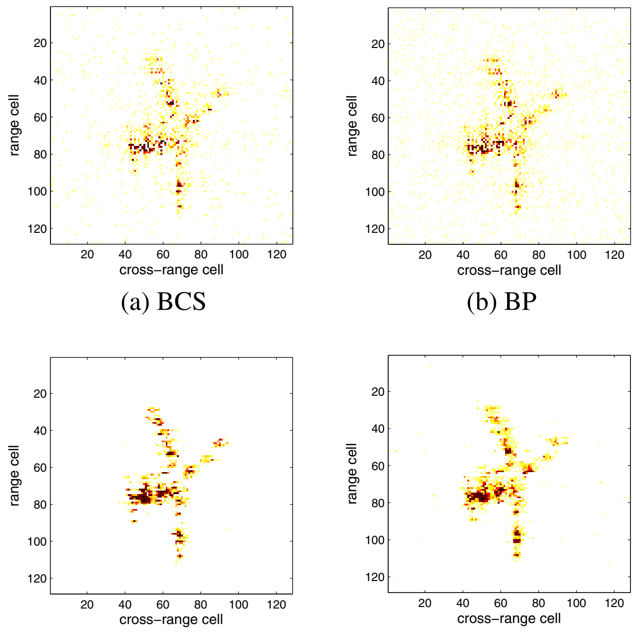

(a) BCS (b) BP

(c) CluSS (d) Algorithm 2

Fig. 4. Comparison of ISAR images.

Table 2. Performance evaluations

Algorithm	BCS	BP	CluSS	Algorithm 2
Correlation	0.7400	0.8009	0.8079	**0.8122**
Entropy	3.2002	0.9844	0.4337	**0.4237**

6. CONCLUSION

The conventional CS-based ISAR imaging methods merely assume that scatterers on target scene are sparse without considering any particular signal structure. In contrast, the proposed approximate imaging algorithm exploits the structural continuity of the scatterers on the target scene in both the cross-range and the range domains. Real data experiments show that the proposed algorithm obtains an enhanced target image in terms of effectively preserving the weak scatterers and removing the noise outside the target region.

7. REFERENCES

[1] V. M. Patel, G. R. Easley, D. M. Healy, Jr., and R. Chellappa, "Compressed synthetic aperture radar," *IEEE J. Sel. Topics Signal Process.*, vol. 4, pp. 244–254, Apr. 2010.

[2] L. Zhang, M. Xing, C. Qiu, J. Li, J. Sheng, Y. Li, and Z. Bao, "Resolution enhancement for inversed synthetic aperture radar imaging under low snr via improved compressive sensing," *IEEE Trans. Geosci. Remote Sens.*, vol. 48, pp. 3824–3838, Oct. 2010.

[3] H. Wang, Y. Quan, M. Xing, and S. Zhang, "Isar imaging via sparse probing frequencies," *IEEE Geosci. Remote Sens. Lett.*, vol. 8, pp. 451–455, May 2011.

[4] M. Çetin and W. Karl, "Feature-enhanced synthetic aperture radar image formation based on nonquadratic regularization," *IEEE Trans. Image Process.*, vol. 10, pp. 623–631, Apr. 2001.

[5] G. Li, H. Zhang, X. Wang, and X. Xia, "Isar 2-d imaging of uniformly rotating targets via matching pursuit," *IEEE Trans. Aerosp. Electron. Syst.*, vol. 48, pp. 1838–1846, Apr. 2012.

[6] G. Xu, M. Xing, L. Zhang, Y. Liu, and Y. Li, "Bayesian inverse synthetic aperture radar imaging," *IEEE Geosci. Remote Sens. Lett.*, vol. 8, pp. 1150–1154, Nov. 2011.

[7] J. Xu, Y. Pi, and Z. Cao, "Bayesian compressive sensing in synthetic aperture radar imaging," *IET Radar, Sonar and Navigation*, vol. 6, pp. 2–8, Jan. 2012.

[8] J. L. Walker, "Range-doppler imaging of rotating objects," *IEEE Trans. Aerosp. Electron. Syst.*, vol. 16, pp. 23–52, Jan. 1980.

[9] L. He and L. Carin, "Exploiting structure in wavelet-based bayesian compressive sensing," *IEEE Trans. Signal Process.*, vol. 57, pp. 3488–3497, Sep. 2009.

[10] L. Yu, H. Sun, J. P. Barbot, and G. Zheng, "Bayesian compressive sensing for cluster structured sparse signals," *Signal Processing*, vol. 92, pp. 259–269, Jan. 2012.

[11] C. P. Robert and G. Casella, *Monte Carlo Statistical Methods*, New York: Springer, 2004.

[12] R.G. Baraniuk, V. Cevher, M.F. Duarte, and C. Hegde, "Model-based compressive sensing," *IEEE Trans. Inf. Theory*, vol. 56, pp. 1982–2001, Apr. 2010.